

This work was written as part of one of the author's official duties as an Employee of the United States Government and is therefore a work of the United States Government. In accordance with 17 U.S.C. 105, no copyright protection is available for such works under U.S. Law.

Public Domain Mark 1.0

<https://creativecommons.org/publicdomain/mark/1.0/>

Access to this work was provided by the University of Maryland, Baltimore County (UMBC) ScholarWorks@UMBC digital repository on the Maryland Shared Open Access (MD-SOAR) platform.

**Please provide feedback**

Please support the ScholarWorks@UMBC repository by emailing [scholarworks-group@umbc.edu](mailto:scholarworks-group@umbc.edu) and telling us what having access to this work means to you and why it's important to you. Thank you.

# An Ultra-Compact, Narrow-Bandwidth, and High-Density Channel Photonic Integrated Channelizer Based on Serial Arrayed Waveguide Grating Architecture

Fabrizio Gambini , Renan Moreira , David Robles , Antonia Gambacorta , and Mark Stephen 

**Abstract**—An ultra-compact, narrow-bandwidth, and high-density photonic integrated channelizer has been developed on a silicon nitride platform and demonstrated for parallel processing of wide band hyperspectral microwave spectra. This device is based on an updated generation of arrayed waveguide gratings (AWG) named serial-AWG (SAWG). The design consists of 33 tunable optical delay lines and 10 output channels. Fabrication inaccuracies are compensated by the use of metal heaters to obtain narrow bandwidth and channel separation, and high side lobe suppression. Our experimental results demonstrate ten 2.6 GHz-bandwidth channels, separated by 3.9 GHz and with 20 dB of side-lobes suppression.

**Index Terms**—Photonic integrated circuit, serial arrayed waveguide grating, wavelength filtering, hyperspectral microwave, channelizer.

## I. INTRODUCTION

INTEGRATED photonics is a breakthrough technology that enables the process of wideband measurement spectra, within an efficient size, weight, power, and cost (SWaP-C). As such, photonic integrated devices have been finding growing applications in different fields such as automotive, communication and sensing. In particular, microwave remote sounding by means of photonic technologies promises to open a new era for hyperspectral microwave measurements from space, with important implications for numerical weather prediction and

climate science [1], [2]. Traditional radiofrequency (RF) technology does not provide a viable solution for the processing of an ultra-wide bandwidth in the microwave domain at hyperspectral resolution ( $< 1$  GHz), due to large SWaP-C constraints. To that end, our team at NASA Goddard Space Flight Center has initiated the development of HyMPI (Hyperspectral Microwave Photonic Instrument): a hyper- and multi-spectral (i.e., hundreds to thousands of spectral channels) microwave sensor by the use of integrated photonic circuits (PIC) to obtain improved Earth remote sensing capabilities [3], [4]. The core of our photonic back end is an optical channelizer. This building block is a filter that requires multiple narrow-bandwidth channels to parallel processing the detected RF spectrum with minimum spectral distortion. In this work, we report the experimental results obtained from an ultra-compact photonic filter based on silicon nitride (SiN) photonic integrated technology. This provides ten ultra-narrow bandwidth (2.6 GHz) channels with 3.9-GHz separation and, at least, 20 dB of side-mode suppression. The device design is based on an updated generation of arrayed waveguide gratings (AWG) named *Serial-AWG* (SAWG) [5], [6]. In the new version, we optimized the design of the optical splitters and heaters, and increased the number of tunable delay lines. The filter consists of 33 tunable delay lines that use platinum (Pt) integrated heaters on top of the photonic waveguides. This solution enables the use of thermo-optical effects to compensate for the optical delay mismatch due to fabrication inaccuracies.

Several passband optical filters have been previously proposed using different platforms and architectural solutions, such as the freespace bulk-optic based filter reported in [7]. These filters can be built with commercial-off-the-shelf parts, with a consequent reduction of the implementation costs, and can achieve a flat-top filtering response, minimizing the distortion of the optical signal. However, the number of channels is limited, and the shape of the filters degenerates to a Gaussian shape for narrow operation bandwidth (less than 10 GHz). Other solutions focus on phase sampled fiber Bragg-grating (FBG) [8] to minimize the filter's footprint, without impacting on the filtering performance (loss, bandwidth and spectral response). Unfortunately, phase sampled FBG filters do not offer tunable solutions, and the fabrication of highly-density multi-channel filters particularly difficult. Single ring resonator PICs provide

Manuscript received 19 September 2023; revised 23 November 2023; accepted 13 December 2023. Date of publication 4 January 2024; date of current version 16 April 2024. This work was supported in part by NASA's Earth Science Technology Office (ESTO) through the NRANNH19ZDA001N, Instrument Incubator Program (IIP), and in part by NASA under Award 80GSFC21M0002. (Corresponding author: Fabrizio Gambini.)

This work did not involve human subjects or animals in its research.

Fabrizio Gambini is with the University of Maryland Baltimore County, Baltimore, MD 21250 USA, also with the Center for Research and Exploration in Space Science and Technology (CREST II), Greenbelt, MD 20771 USA, and also with the NASA Goddard Space Flight Center, Greenbelt, MD 20771 USA (e-mail: fgambini@umbc.edu).

Renan Moreira is with the Ultra-Low Loss Technologies, Goleta, CA 93117 USA (e-mail: renan.moreira@ulltechnologies.com).

David Robles, Antonia Gambacorta, and Mark Stephen are with the NASA Goddard Space Flight Center, Greenbelt, MD 20771 USA (e-mail: david.j.robles@nasa.gov; antonia.gambacorta@nasa.gov; mark.a.stephen@nasa.gov).

Color versions of one or more figures in this article are available at <https://doi.org/10.1109/JLT.2024.3349932>.

Digital Object Identifier 10.1109/JLT.2024.3349932

TABLE I  
COMPARISON OF PERFORMANCE METRICS FOR SEVERAL STATE-OF-THE-ART PHOTONIC FILTER ARCHITECTURES AND THE PROPOSED SAWG

Ref.	Central wavelength [nm]	Num. of output	Bandwidth [GHz]	Channels separation [GHz]	Side-mode suppression [dB]	Waveguide loss [dB/cm]	Footprint [mm <sup>2</sup> ]	Num. of active controls	Architecture type	Filter shape
[12]	1550	16	1	1	12.5	1	0.65	14	MZI	Gaussian
[15]	1550	11	1	1	15	3	1.1	35	AWG	Gaussian
[19]	1560	8	160	380.9	38.9	> 39	0.5	0	AWG	Gaussian
[20]	850	160	< 30	50	26.8	0.5	25	0	AWG	Gaussian
[21]	N/A	16	25	1.6	N/A	0.02	N/A	16	AWG	Gaussian
[22]	1550	30	19	200	22	< 0.1	10.8	0	AWG	Gaussian
This work	1550	10	2.8	3.9	20	0.2	2.43	33	SAWG	Improved Gaussian (experimentally demonstrated) Flat-top (theoretically demonstrated)

a viable solution when it comes to passband filters with few controls. However, these solutions generate Lorentzian filtering shapes which are responsible for decreasing channel selectivity. For this reason, resonating structures have been designed [9] and developed [10], [11] using different ring resonators. While improving filter SWaP-C, these solutions enable generating multiple tunable channels with flat-top spectral responses and improved selectivity. However, they all require a larger number of controls due to the multiple rings per channel. Moreover, narrow-bandwidth ring filters in parallel coupled configuration require additional controls to optimize the optical delay introduced by the waveguides connecting the rings input/output ports. The number of controls poses a limitation on the scalability of the system. Finally, narrow-bandwidth solutions can be severely affected by fabrication constraints and inaccuracies on the optical loss and couplers' splitting ratio. Different architectures based on Mach-Zehnder interferometer (MZI) enable multiple output channels with a lower number of controls, however it is difficult to obtain high extinction ratios and a filtering response different from Gaussian shape [12].

Photonic integrated AWGs are common planar devices that offer multiplexing/demultiplexing functionalities in wavelength division multiplexing (WDM) schemes [13]. This design requires an input star coupler to divide the optical input power into an array of waveguides with different phase delays. A second star coupler recombines the output from the delay lines. Narrow bandwidth and high density channel AWGs are characterized by a large number of waveguides in the array. The optical delay of each waveguide needs to be accurately calculated to optimize the filter response. However, the fabrication inaccuracies affect the optical length of the waveguides, introducing phase errors that alter the spectral performance [14]. [15] developed an 11-channel AWG with active phase correction using 1 GHz channel spacing and 15 dB side-mode suppression. This architecture, on the other hand, does not allow for a flat-top filtering response. Our previous work [5] introduced an alternate AWG design. The SAWG design utilizes heaters on top of its 17 delay lines to compensate for fabrication inaccuracies. This solution exhibits limited inter-channel cross-talk, with a bandwidth and channel separation of 4.5 GHz. Similar AWG designs, with reusable

delay lines, have been proposed for a lower number of filtering channels, coarser bandwidth and channel separation [16], [17] or for narrow bandwidth channels but with the support of serpentine integrated grating and external lenses that worsen the fabrication complexity and the integration [18]. Table I proposes a summary on the state-of-the-art in photonic filters performance. The SAWG architecture proposed in this work provides narrow-bandwidth and high-density channel filters with improved passband selectivity and filter shape.

## II. DEVICE ARCHITECTURE AND DESIGN

Fig. 1 reports the generic SAWG architecture. The device consists of a single long delay line with  $N$  tunable directional couplers (DC) and one star coupler (SC). The DCs split fractions of the optical signal in the delay line, and the SC performs the Fourier transform of the input distribution. Each DC has been designed to provide a power splitting ratio ( $K_i$ ). The signals at the output of the different DCs arrive to the SC with an intensity and an optical delay which are related to the  $K_i$  values and the length of the optical path traveled in the delay line, respectively. The SC performs the Fourier transform of the signal distribution at the input ports. For this reason, the control of the  $K_i$  values and the optical delay is the key to optimize the filter response in terms of shape, bandwidth, rejection, and channel separation. This feature is impossible to obtain using a standard AWG design, since the first SC splits the input signals with a Gaussian distribution at its own output ports. Fig. 2 reports some examples that demonstrate the effect of the splitting ratios on the filter performance for a SAWG with 17-input SC. Three different intensity distributions at the SC's input ports (Fig. 2(a)–(c), left) generate different filtering shapes (Fig. 2(d)–(e), right). Fig. 2(a) reports a case in which the DCs enable a uniform intensity distribution, while Fig. 2(b) shows a non-uniform Gaussian distribution at the 17 input ports of the SC. An interesting case is reported in Fig. 2(c) which describes a 17-points sinc function distribution. Fig. 2(d) shows that the uniform intensity distribution enables a filter's main lobe with a round passband shape and limited side lobe suppression. Theoretically, the Fourier transform of a constant signal is a delta function however, the finite number of points (or

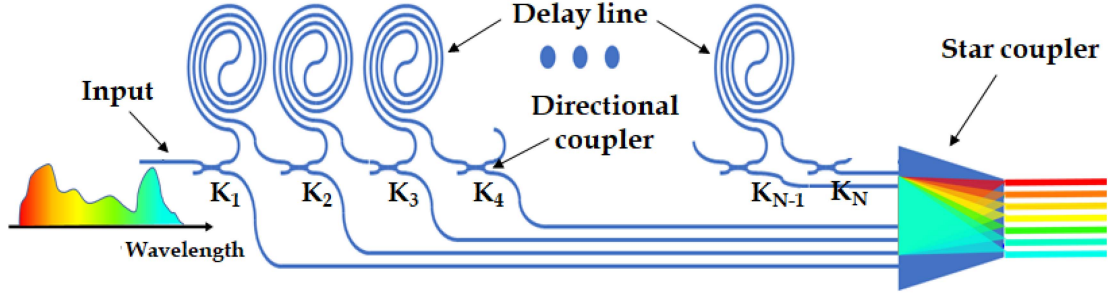


Fig. 1. Generic serial arrayed waveguide grating architecture showing the delay line, the directional couplers and the respective splitting ratio values ( $K_i$ , for  $i = 1, \dots, N$ ) and the star coupler.

SC input ports) limits the shape and the side-mode suppression. The result obtained in Fig. 2(e) is related to the Gaussian input distribution. This solution improves the side-mode suppression, but the main lobe maintains a round passband shape. On the other hand, the filter shape reported in Fig. 2(f) and related to the sinc function intensity distribution, enables a flat-top response and this introduces a minimum distortion of the signal in the passband. In this example the secondary lobes are still high, but their intensity can be lowered with a higher number of SC input ports. The proposed SAWG has been implemented considering 33 SC input ports. Another important benefit introduced by this innovative architecture is the access to the optical delays of the filter without compromising the footprint of the circuit. In the standard AWG architecture the waveguides in the array are kept close to reduce the footprint and to maintain a suitable delay length. However, the fabrication inaccuracies on the waveguides can generate significant delay mismatches with a consequent degradation of the optical filtering performance. For this reason, it is important to independently control the delay of the signals in the array, in order to maximize the performance of the channelizer. In our proposed SAWG scheme it is possible to space the waveguides to introduce optical delay tuning elements, such as metallic heaters to the circuit layout. Fig. 3(a) shows the microscope image of the fabricated SAWG. The PIC was manufactured at Ultra-Low Loss Technologies (Santa Barbara, USA) as a part of a SiN wafer run. The cross-section of the SiN waveguide is a 175 nm-thick and 1.8  $\mu\text{m}$ -wide strip (see Fig. 3(b)). The optical loss are below 0.2 dB/cm. The SiN waveguides support at least one transverse magnetic (TM) and one transverse electric (TE) propagating modes. However, in order to optimize the performance of the device, only the TE is allowed in the circuit. For this reason, a mode-filter is added at the input port in order to reject the TM mode and sustain only the TE mode. The mode-filter consists of a 100  $\mu\text{m}$ -radius and 1.5  $\mu\text{m}$ -wide s-bend waveguide. A 150  $\mu\text{m}$ -long linear taper minimizes the optical loss at the interface with the 1.8  $\mu\text{m}$ -wide edge coupler and SAWG input waveguides. The fabrication constraints limit the minimum gap between the waveguides at 500 nm. Finite-difference time-domain (FDTD) analysis has been performed on both symmetric and asymmetric DC configurations (Fig. 7(b)). Symmetric DCs show  $K_i \geq 11\%$  for coupling lengths  $L_{DC} \geq 0 \mu\text{m}$ , due to the s-bends transitions. For

this reason, asymmetric DCs are used to achieve lower splitting ratios.

Fig. 4(a) reports the 33  $K_i$  values that enable a sinc function intensity distribution at the input of the SC, as shown in Fig. 4(b). The color of the points indicates the configuration of the DCs along the delay line: red for asymmetric and blue for symmetric. The analysis performed using our model indicates that a 33-input SC provides an improvement of the channel selectivity compared to the Gaussian filtering shape provided by the standard AWG design. The SC has been designed to provide 10 output channels to cover a 40 GHz-range in the optical domain. The footprint of the PIC is  $12.5 \times 19.5 \text{ mm}^2$  and it is related to the SiN platform selected for the fabrication of the PICs which limits the minimum waveguide bending radius to 200  $\mu\text{m}$ . Two sets of 38 (north) and 36 electrical pads (south) are used to control the optical delays and the splitting ratios, while 15 edge couplers are used to measure the light from the PIC. The optical and electrical interfaces have been designed to ease the packaging of the chip. The filter channels have been designed to operate around 1550 nm, with 4 GHz channel separation, below 3 GHz channels' bandwidth and 20 dB of side-mode suppression.

#### A. Tunable Delay Lines

Platinum (Pt) heaters have been designed above the waveguides at the input of the SC to vary the optical delays by modifying the effective index of the propagating optical mode. Finite-element method (FEM) simulations were performed to maximize the thermo-optic efficiency. Fig. 5 shows the example of a temperature gradient across the tunable optical waveguide cross-section. The optical delay of each signal at the SC input ports, can be independently tuned with a 22  $\mu\text{m}$ -wide and 14 mm-long Pt heater. The thickness of the upper cladding is 3  $\mu\text{m}$  as reported in Fig. 3(b). This should ensure a negligible interaction between the tail of the optical waveguide mode and the metal.

Fig. 6 reports the FEM model results. The maximum waveguide temperature variation is 14°C for 1 W of dissipated electrical power. Considering the cross-section and the refractive indices of the materials involved, the group index variation, calculated using our electro-magnetic mode model, is about  $2.0 \cdot 10^{-5} \text{ } ^\circ\text{C}^{-1}$  at 1550 nm, for a 1.8  $\mu\text{m}$ -wide and 175 nm-thick



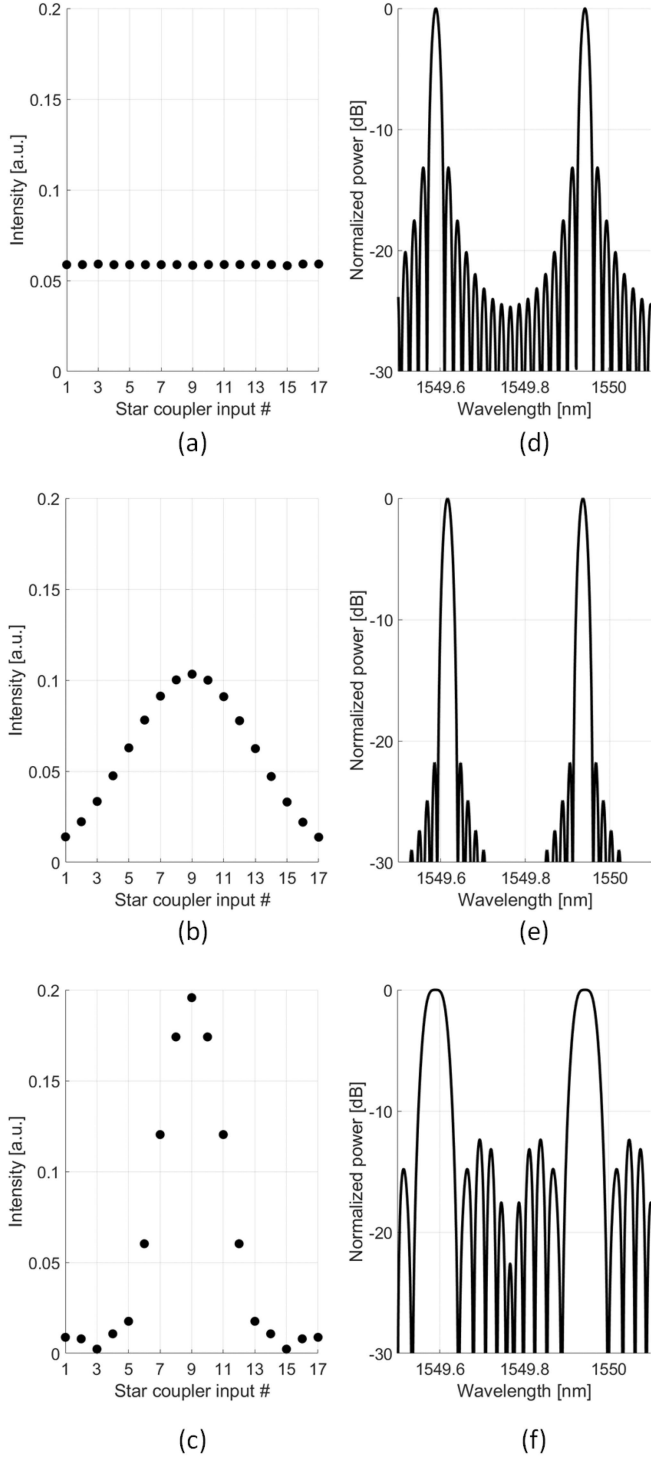


Fig. 2. Effect of different intensity input distributions at the star coupler (left): (a) uniform, (b)–(c) non-uniform, and the respective spectra response of the serial arrayed waveguide grating (right): (d)–(f).

waveguide. With these assumptions, the total group delay can be tuned up to 13 fs and this ensures optical delays that correspond to signal phase variation of about  $5\pi$  [rad]. The heaters on the optical waveguides (WG heater) are separated by  $34.8 \mu\text{m}$  to minimize the thermal crosstalk.

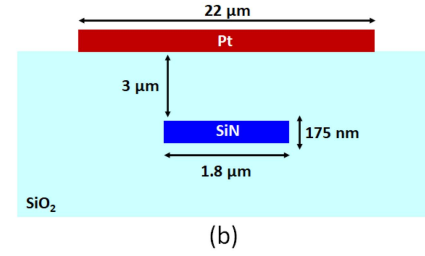
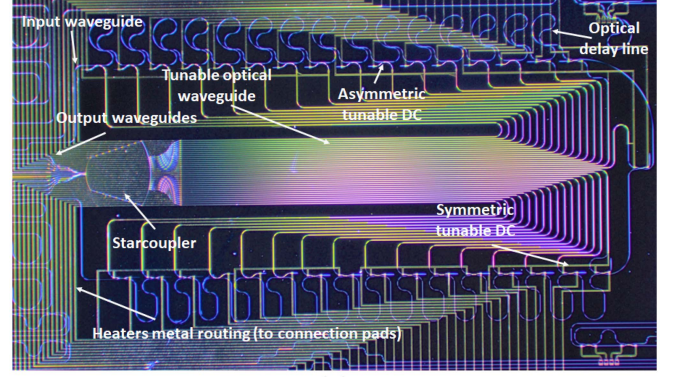


Fig. 3. (a) Microscope photo of the serial arrayed waveguide grating photonic integrated circuit with building block names, (b) silicon nitride waveguide cross-section.

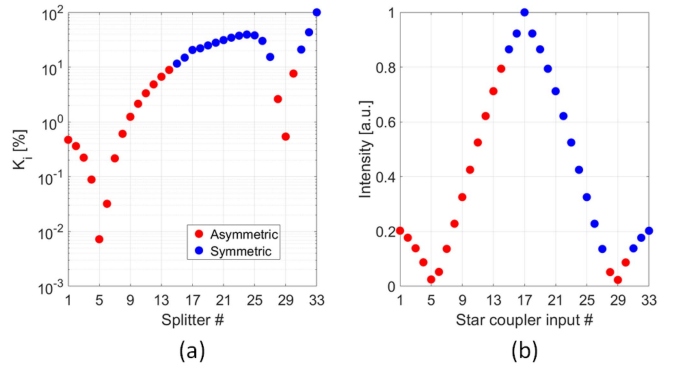


Fig. 4. Splitting ratio values for the asymmetric (red) and symmetric (blue) directional coupler configurations (a) and the intensity distribution at the star coupler's input ports (b).

### B. Tunable Directional Couplers

The fabrication inaccuracies can also affect the splitting ratio of the DCs. In our architecture the  $K_i$  values need to be optimized in order to limit the distortions of the output transfer function of the SAWG. For this reason, one of the DC coupled waveguides is supported with a  $5.8 \mu\text{m}$ -wide laterally shifted Pt heater [23] to maximize the temperature gradient and induce the highest phase velocity mismatch between the coupled optical modes. This effect enables the tuning of the DCs and it can be used to compensate the impact of the fabrication errors on the  $K_i$  values. Fig. 7 shows the offset heater on the DC (DC heater). FEM simulations have been performed to optimize the tunability efficiency. FEM results suggested a  $4.2 \mu\text{m}$ -shift from the center

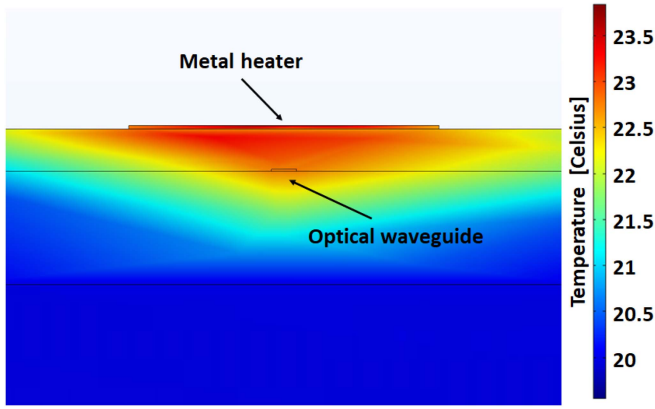


Fig. 5. Example of FEM simulation results, showing the temperature gradient across the tunable optical waveguide cross-section.

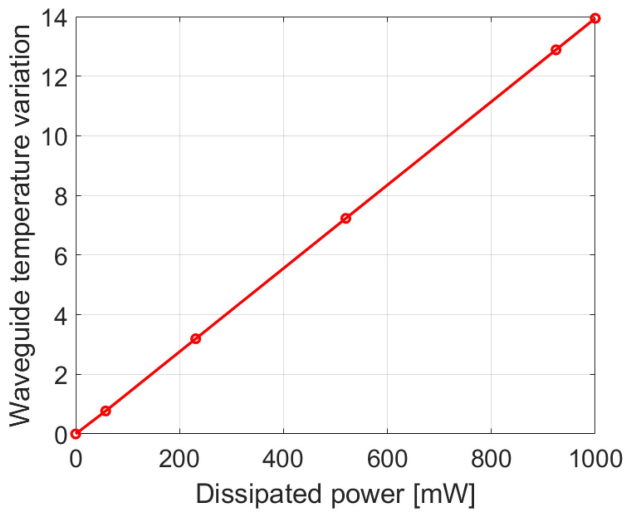


Fig. 6. Waveguide temperature variation as a function of the 22  $\mu\text{m}$ -wide and 14 mm-long heater dissipated powers.

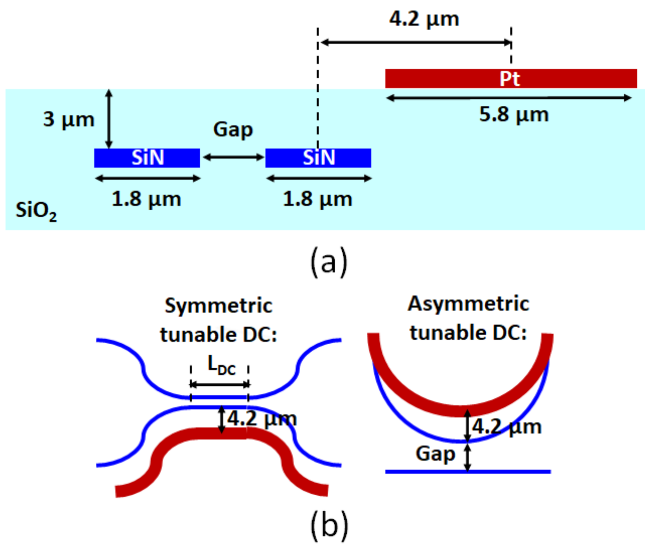


Fig. 7. (a) Cross-section of the tunable directional couplers, and (b) on-top view schematics for the tunable symmetric and asymmetric tunable directional couplers with offset heaters.

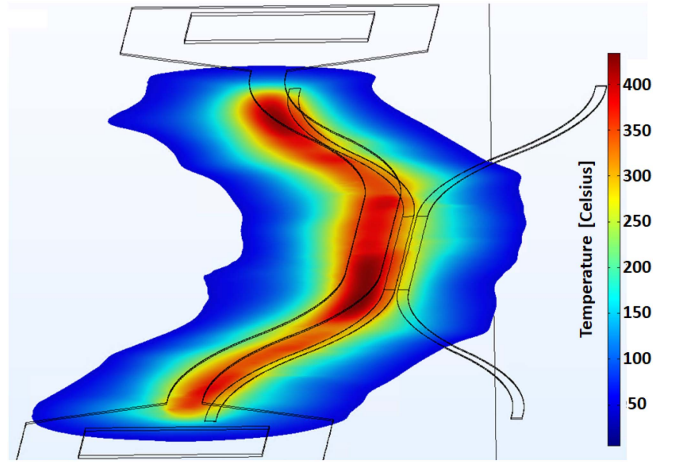


Fig. 8. Example of FEM simulation results, showing the temperature gradient at the waveguide level between the coupled waveguides.

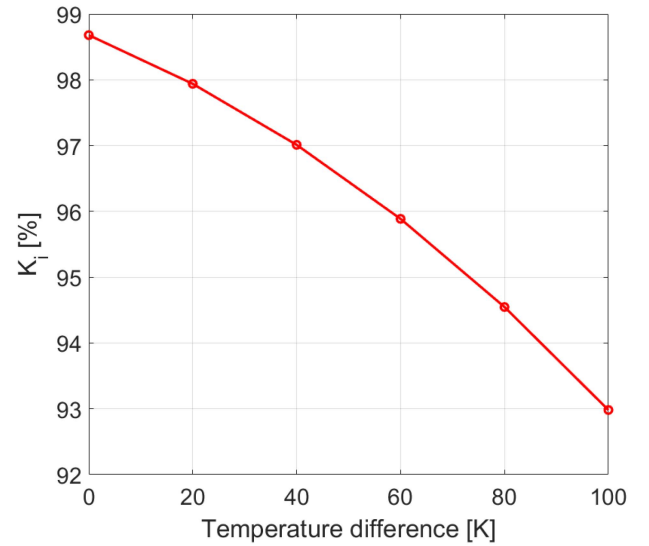


Fig. 9. Example of simulated splitting ratio evolution as function of the temperature gradient between two straight 500 nm-gap 80  $\mu\text{m}$  coupling length.

of the coupled waveguides to the center of the heater. The low thermo-optical coefficient of the SiN waveguides limits the performance of tunable DC. However, the silica ( $\text{SiO}_2$ ) provides a good thermal isolation and this enhances the temperature gradient between the coupled waveguides, which are already separated by 500 nm or more. The FEM example reported in Fig. 8 demonstrates the temperature difference between the two waveguides which enables the tuning of the coupler. Fig. 9 shows an example of simulation results obtained with two straight 80  $\mu\text{m}$ -long coupled waveguides. A temperature variation of 100°C changes the splitting ratio from about 99% down to 93%.

### III. EXPERIMENTAL RESULTS AND DISCUSSION

Fig. 10 shows the test setup for the characterization of the SAWG performance. An external cavity tunable laser (TL)

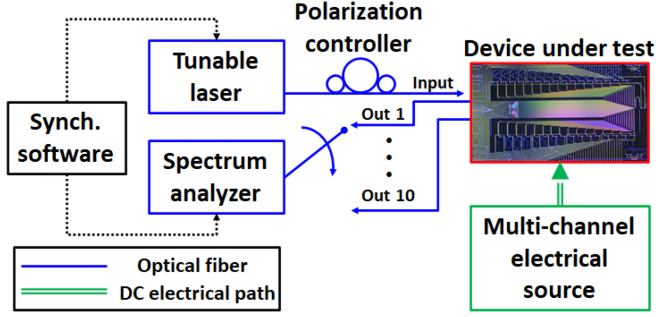


Fig. 10. Experimental setup for spectrum characterizations.

generates a continuous wavelength between 1547.5 nm and 1552.5 nm with a power of 10 dBm. A polarization controller is used to align the polarization of the injected light. The output spectra are recorded with a spectrum analyzer synchronized with the TL. A 16-port fiber array with ultra-high numerical aperture (UHNA) fibers, aligned on the side of the PIC, couples the light in and out from the PIC. UHNA are used to limit the coupling loss due to the optical mode mismatch between the fibers and the non-tapered edge couplers. Two alignment loops enable the proper alignment of the fiber array. The chips are characterized at room temperature. Two direct-current multi-probes connected with the electrical pad arrays inject the electrical current in the integrated resistive heaters. The electrical signals are generated by a multi-channel electrical source. The current-voltage (IV) characteristics have been measured for all the metal heaters on top of the delay lines. Higher voltage results in higher dissipated power and increased temperature of the metal. This also translates in a variation of the resistivity as described in (1) [24]:

$$\rho = \rho_0(1 + \alpha\Delta T) \quad (1)$$

where  $\alpha$  is the temperature coefficient of resistance of Pt (equal to  $2.9771 \cdot 10^{-3} \text{ } ^\circ\text{C}^{-1}$  [25]),  $\Delta T$  is the temperature difference and  $\rho_0$  is the resistivity at the initial temperature  $T = T_0$ . The measured average resistance of the WG heaters is 460  $\Omega$ . Fig. 11(a) and (b) reports the measurement results of the DCs test structures for both the symmetric and asymmetric configurations, respectively. The  $K_i$  values of the symmetric DCs have been evaluated using the method in [26] (red circles), for coupling lengths ( $L_{DC}$ ) shorter than 50  $\mu\text{m}$ . In this method, the splitting ratio of the DCs is characterized by measuring the extinction ratio of an unbalanced MZI (UMZI) composed with the same DCs and compare the results with the UMZI mathematical model. Symmetric DCs with longer coupling lengths were not designed in UMZI schemes, so their  $K_i$  values were estimated by calculating the optical power ratio at their output ports (red diamonds). In both configurations the results show very small discrepancies compared to the 3D-FDTD analysis. Fig. 12 demonstrates that the DC splitting ratio can be optimized by applying voltage on the DC heater. The  $K_i$  value is reduced down to 97.57% for 7 V of applied voltage. It is worth mentioning that, since the measured splitting characteristics reported in Fig. 11 shows a

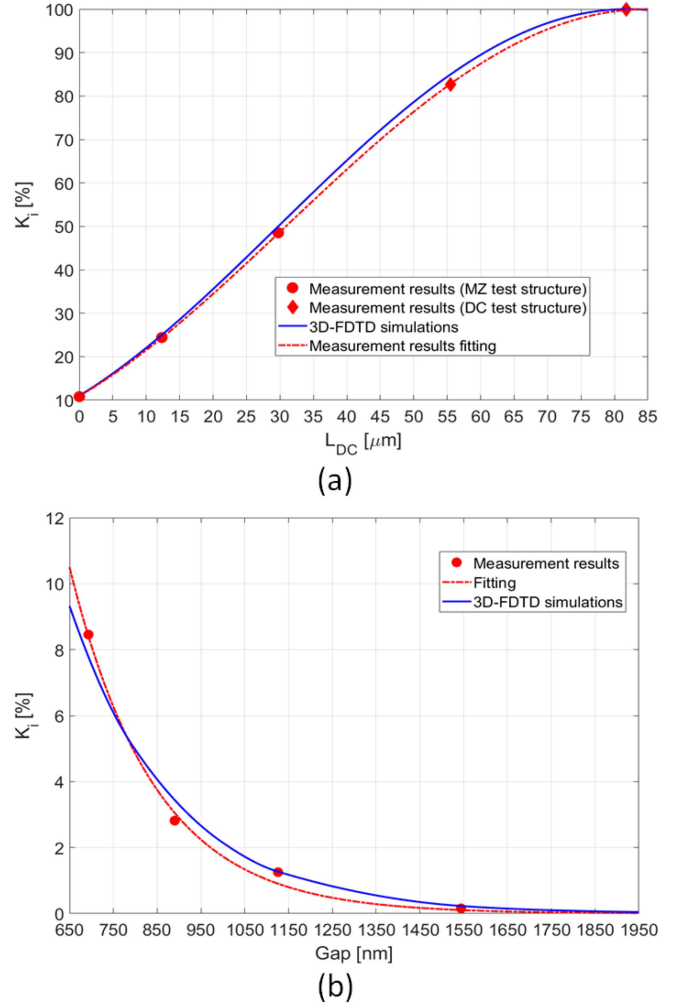
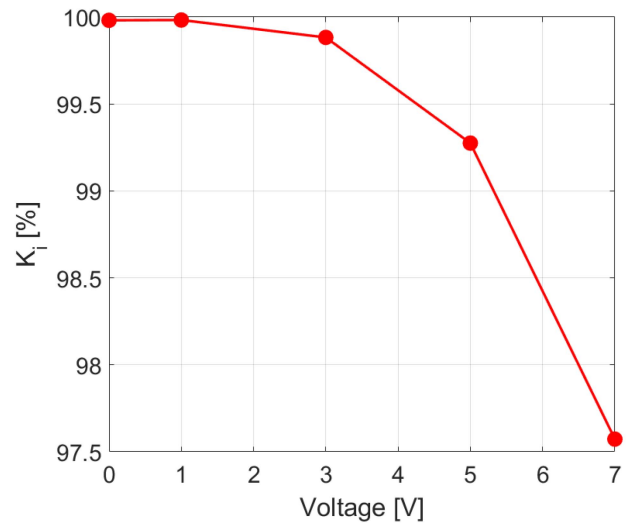


Fig. 11. Splitting ratios for symmetric (a) and asymmetric (b) directional couplers, as a function of the coupling length and waveguide gap respectively.

Fig. 12. Example of measured splitting ratio variation as function of the applied voltage on the 500 nm-gap 81.751  $\mu\text{m}$ -long DC heater.



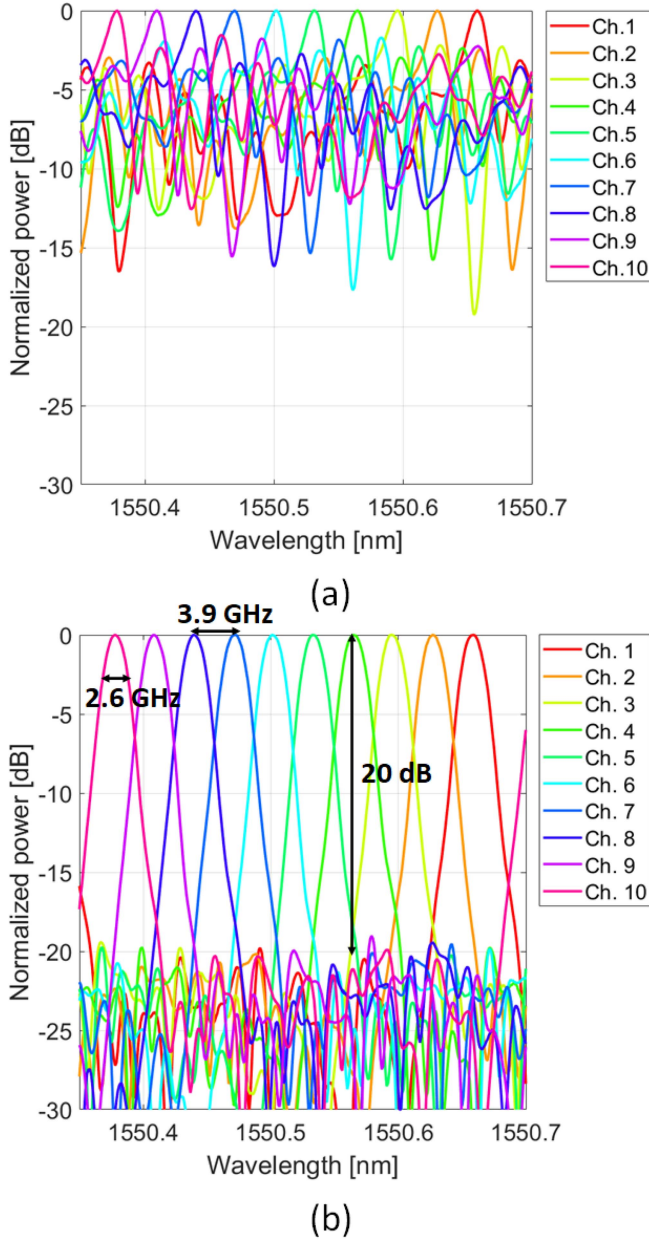


Fig. 13. Measured output spectra of the serial arrayed waveguide grating without (a) and with optical delay errors compensation (b).

high agreement with the theoretical results, the filter spectra response presented here have been obtained without the tuning of the DCs. Fig. 13(a) reports the spectra measured at the output ports of the SAWG, when no WG heater is activated. In this scenario, the filtering response is compromised by the fabrication inaccuracies. The re-alignment of the optical delays is obtained by scanning the applied voltage of each WG heater and fixing the value that ensures the maximum output power, for a fixed wavelength, at the SAWG output port [15]. For this purpose, the WG heaters were sequentially tuned by ranging the applied voltage from 0 V to 20 V. At every step, the optical power was recorded. Each WG heater was set to the voltage value that maximizes the optical transmission. This method is

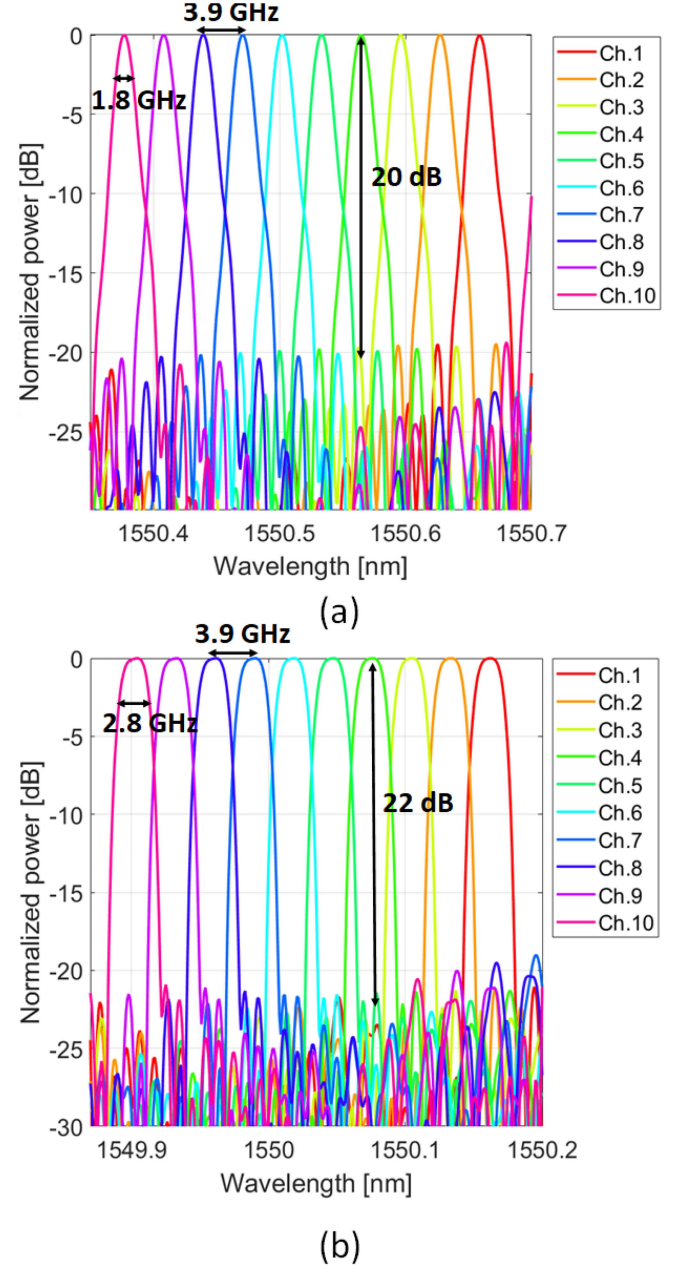


Fig. 14. Simulated output spectra of the serial arrayed waveguide grating after optical delay errors compensation (a) and after optical delay errors compensation with an additional  $\pi$  [rad] phase variation on channels 1-5 and 29-33 for flat-top response (b).

easy to implement but it requires an analysis time that depends on the voltage step. The manual fiber array alignment stage used in the setup drifts over long period of time, and this introduces errors in the decision of the optimal operating point during the WG heaters analysis. Our calculations suggest that a 0.1 V-step should be used to fully optimize the filtering performance of the device. However, to demonstrate the capabilities of the SAWG while maintaining an analysis time suitable for the fiber array alignment stage, a step of 0.5 V was chosen. The results, shown in Fig. 13(b) for all 10 output channels, demonstrate the ability of the SAWG to fully recover from the fabrication errors in the



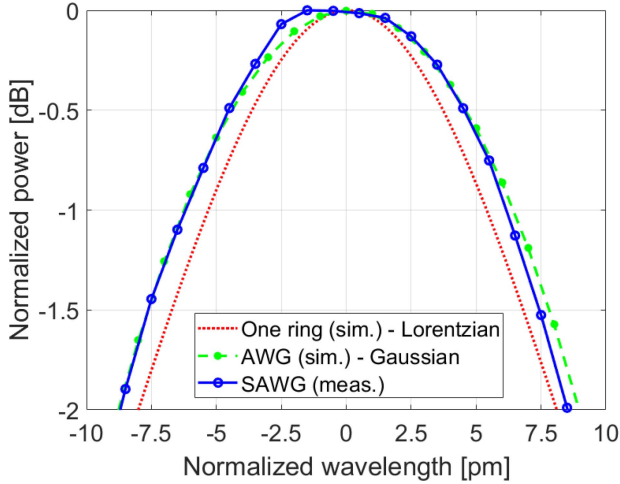


Fig. 15. SAWG measured filter shape (solid blue line), obtained after an additional  $\pi$  [rad] phase variation on delay lines: 1-5 and 29-33, compared to Lorentzian (dot red line) and Gaussian (dash green line) simulated filter responses from single ring and AWG filters respectively, with similar bandwidth.

optical waveguides. The -3 dB bandwidth is about 2.6 GHz per channel and the side mode suppression is 20 dB. The channels are separated by 3.9 GHz. The small discrepancy between the theoretical (4 GHz) and measured (3.9 GHz) channel separation is related to the fabrication inaccuracies on the thickness and width of the waveguides, which affect the group index. The SAWG insertion loss is about 14.2 dB, and the measured coupling loss between the UHNA fibers and the PIC waveguides is 3.9 dB/interface. The current design of the star coupler reduces the footprint of the device, but from our analysis, it introduces about 10 dB of excess loss.

Fig. 14(a) shows the simulated spectra after the phase error compensation and it has been obtained through a transfer-function-based model of the SAWG. The channel separation and -3 dB bandwidth are 3.9 GHz and 1.8 GHz, respectively. This result demonstrates the capability of our model to predict the optical performance of the SAWG with high accuracy. Further analysis indicate that, by applying a phase variation equal to  $\pi$  [rad], in the first- and last-five delay lines, the signal distribution at the input of the SC (see Fig. 4(b)) becomes a truncated sinc function. In this scenario, our model predicts a flat-top filtering response with a slight increment of the channel bandwidth, as demonstrated in the results shown in Fig. 14(b). Fig. 15 shows the comparison of the passband filter shapes between the measured SAWG (solid blue line, obtained after an additional  $\pi$  [rad] phase variation on delay lines: 1-5 and 29-33), the Gaussian (dash green line) and Lorentzian (dot red line) provided by a simulated AWG and single ring filters with similar bandwidth. The SAWG spectrum could not be fully optimized due to the remaining residual phase error related to the coarse voltage step used for the WG heaters. Nonetheless, a more flat response is registered. A better stability of the fiber array alignment will allow a finer resolution for the WG heaters analysis with a consequent benefit for the selectivity and shape of the SAWG spectral response.

#### IV. CONCLUSION

A photonic integrated channelizer based on a SiN SAWG has been designed, fabricated and experimentally demonstrated. FEM and 3D-FDTD simulations have been performed to optimize the electro-optical capabilities of the device and a transfer-function-based model has been developed to predict the filtering shape of the system. 33 integrated WG heaters can be independently activated to thermally tune the delays and optimize the filter's optical performance. Ten 2.6 GHz-bandwidth optical channels separated by 3.9 GHz with 20 dB side-mode suppression have been demonstrated thanks to the innovative architecture, which enables the compensation of the phase error introduced by the fabrication inaccuracies on the optical delay lines. The experimental setup used for the test does not allow to find the proper configuration of the WG heaters. The time required to find the optimal operating point for the single WG heater is not suitable for the manual fiber array alignment stage used in the experimental setup. Its stability and consequently the coupling efficiency between the fiber array and the input/output PIC waveguides cannot be guaranteed for the long period of time required to perform a fine tuning of the WG heaters. The fiber array misalignment introduces errors in the decision of the optimal operating configuration of the WG heaters. To minimize the analysis time a 0.5 V voltage resolution has been used. While this value is appropriate to recover the filter shape and demonstrate a narrow and dense filter operation with high side-mode suppression, the remaining phase error affects the ability to fully demonstrate the circuit capabilities in terms of bandwidth and filter shape. Current experimental setup limitations notwithstanding, the passband filter shape is observed to reduce the distortion with an improved Gaussian shape response.

Based on our simulations, we expect the packaged version of the SAWG to meet a 10 flat-top, 4 GHz-bandwidth channel specification. The PIC is currently under packaging service and the results reported in this work are related to the un-packaged version of the SAWG.

#### REFERENCES

- [1] C. Turner, M. Stephen, F. Gambini, G. Chin, P. Racette, and T. Murphy, "Ultra-wideband photonic radiometer for submillimeter wavelength remote sensing," in *Proc. IEEE Int. Topical Meeting Microw. Photon.*, 2020, pp. 124–127, doi: [10.23919/MWP48676.2020.9314456](https://doi.org/10.23919/MWP48676.2020.9314456).
- [2] A. Gambacorta et al., "Advancing atmospheric thermodynamic sounding from space using hyperspectral microwave measurements," *IEEE J. Sel. Topics Appl. Earth Observ. Remote Sens.*, vol. 16, pp. 5204–5218, 2023, doi: [10.1109/JSTARS.2023.3269697](https://doi.org/10.1109/JSTARS.2023.3269697).
- [3] A. Gambacorta et al., "The hyperspectral microwave photonic instrument (HYMPI) - advancing our understanding of the earth's planetary boundary layer from space," in *Proc. IEEE Int. Geosci. Remote Sens. Symp.*, 2022, pp. 4468–4471, doi: [10.1109/IGARSS46834.2022.9883151](https://doi.org/10.1109/IGARSS46834.2022.9883151).
- [4] A. Gambacorta et al., "The hyperspectral microwave photonic instrument (HYMPI)," in *Proc. IEEE Int. Geosci. Remote Sens. Symp.*, 2022, pp. 7206–7209, doi: [10.1109/IGARSS46834.2022.9884548](https://doi.org/10.1109/IGARSS46834.2022.9884548).
- [5] F. Gambini, R. Moreira, A. Gambacorta, J. Klamkin, and M. Stephen, "An innovative photonic integrated channelizer design for hyperspectral microwave sounding," in *Proc. OSA Opt. Sensors Sens. Congr.*, 2021, paper HF4E.5.
- [6] M. Stephen, R. Moreira, and F. Gambini, "Serial arrayed waveguide grating," U.S. Patent US11852864B1, Dec. 26, 2023.

- [7] E. Pincemin et al., "Multi-band OFDM transmission at 100 gbps with sub-band optical switching," *J. Lightw. Technol.*, vol. 32, no. 12, pp. 2202–2219, Jun. 2014, doi: [10.1109/JLT.2014.2322517](https://doi.org/10.1109/JLT.2014.2322517).
- [8] X. Zou, M. Li, W. Pan, L. Yan, and L. Shao, "Multichannel narrow, flat-top optical filters based on multiple-phase-shifted and phase sampled FBG," *IEEE J. Quantum Electron.*, vol. 53, no. 1, pp. 1–5, Feb. 2017, doi: [10.1109/JQE.2016.2640218](https://doi.org/10.1109/JQE.2016.2640218).
- [9] A. Melloni, "Synthesis of a parallel-coupled ring-resonator filter," *Opt. Lett.*, vol. 26, no. 12, pp. 917–919, 2001, doi: [10.1364/OL.26.000917](https://doi.org/10.1364/OL.26.000917).
- [10] Y. Ding et al., "Thermo-optic tunable optical filters with GHz-bandwidth and flat-top passband on thin film lithium niobate platform," *Opt. Exp.*, vol. 30, no. 12, pp. 22135–22142, 2022, doi: [10.1364/OE.458218](https://doi.org/10.1364/OE.458218).
- [11] Q. Fang et al., "Multi-channel silicon photonic receiver based on ring-resonators," *Opt. Exp.*, vol. 18, no. 13, pp. 13510–13515, 2010, doi: [10.1364/OE.18.013510](https://doi.org/10.1364/OE.18.013510).
- [12] C. H. Chen and Y.-J. Hung, "5 GHz optical channelizer based on cascaded mach-zehnder interferometers on SOI," in *Proc. IEEE 27th OptoElectronics Commun. Conf. Int. Conf. Photon. Switching Comput.*, 2022, pp. 1–3, doi: [10.23919/OECC/PSC53152.2022.9849878](https://doi.org/10.23919/OECC/PSC53152.2022.9849878).
- [13] D. Dai et al., "Low-loss Si<sub>3</sub>N<sub>4</sub> arrayed-waveguide grating (de)multiplexer using nano-core optical waveguides," *Opt. Exp.*, vol. 19, no. 15, pp. 14130–14136, 2011, doi: [10.1364/OE.19.014130](https://doi.org/10.1364/OE.19.014130).
- [14] T. Goh, S. Suzuki, and A. Sugita, "Estimation of waveguide phase error in silica-based waveguides," *J. Lightw. Technol.*, vol. 15, no. 11, pp. 2107–2113, Nov. 1997, doi: [10.1109/50.641530](https://doi.org/10.1109/50.641530).
- [15] M. Gehl, D. Trotter, A. Starbuck, A. Pomerene, A. L. Lentine, and C. DeRose, "Active phase correction of high resolution silicon photonic arrayed waveguide gratings," *Opt. Exp.*, vol. 25, no. 6, pp. 6320–6334, 2017, doi: [10.1364/OE.25.006320](https://doi.org/10.1364/OE.25.006320).
- [16] J. Zhan, Y. Zhang, W.-L. Hsu, S. Veilleux, and M. Dagenais, "Design and implementation of a Si<sub>3</sub>N<sub>4</sub> three-stigmatic-point arrayed waveguide grating with a resolving power over 17,000," *Opt. Exp.*, vol. 31, no. 4, pp. 6389–6400, 2023, doi: [10.1364/OE.480823](https://doi.org/10.1364/OE.480823).
- [17] Y. Zhang, J. Zhan, S. Veilleux, and M. Dagenais, "Arrayed waveguide grating with reusable delay lines (RDL-AWG) for high resolving power, highly compact, photonic spectrographs," in *Proc. IEEE Photon. Conf.*, 2022, pp. 1–2, doi: [10.1109/IPC53466.2022.9975744](https://doi.org/10.1109/IPC53466.2022.9975744).
- [18] M. Brand et al., "High-resolution and compact serpentine integrated grating spectrometer," *J. Opt. Soc. Amer. B*, vol. 38, pp. A75–A85, 2021, doi: [10.1364/JOSAB.423968](https://doi.org/10.1364/JOSAB.423968).
- [19] M. Piels, J. F. Bauters, M. L. Davenport, M. J. R. Heck, and J. E. Bowers, "Low-loss silicon nitride AWG demultiplexer heterogeneously integrated with hybrid III-V/Silicon photodetectors," *J. Lightw. Technol.*, vol. 32, no. 4, pp. 817–823, 2014, doi: [10.1109/JLT.2013.2286320](https://doi.org/10.1109/JLT.2013.2286320).
- [20] D. Seyringer et al., "Technological verification of size-optimized 160-channel silicon nitride-based AWG-spectrometer for medical applications," *Appl. Phys. B*, vol. 125, no. 88, 2019, doi: [10.1007/s00340-019-7192-1](https://doi.org/10.1007/s00340-019-7192-1).
- [21] H. I. West, J. Murakowski, and D. W. Prather, "Fiber-based arrayed waveguide grating for spectral sensing," *Proc. SPIE*, vol. 12000, pp. 90–95, 2022, doi: [10.1117/12.2610329](https://doi.org/10.1117/12.2610329).
- [22] Z. Zhang et al., "High-performance integrated photonic spectrometers based on arrayed waveguide gratings in silica," *Proc. SPIE*, vol. 10706, pp. 999–1005, 2018, doi: [10.1117/12.2311856](https://doi.org/10.1117/12.2311856).
- [23] P. Orlandi, F. Morichetti, M. J. Strain, M. Sorel, A. Melloni, and P. Bassi, "Tunable silicon photonics directional coupler driven by a transverse temperature gradient," *Opt. Lett.*, vol. 38, no. 6, pp. 863–865, 2013, doi: [10.1364/OL.38.000863](https://doi.org/10.1364/OL.38.000863).
- [24] C. Feldman, "Temperature dependency of resistance of thin metal films," *J. Appl. Phys.*, vol. 34, pp. 1710–1714, 1963, doi: [10.1063/1.1702665](https://doi.org/10.1063/1.1702665).
- [25] M. Schepperle, M. Ghanam, A. Bucherer, T. Gerach, and P. Woias, "Non-invasive platinum thin-film microheater/temperature sensor array for predicting and controlling flow boiling in microchannels," *Sensors Actuators A: Phys.*, vol. 345, 2022, Art. no. 113811, doi: [10.1016/j.sna.2022.113811](https://doi.org/10.1016/j.sna.2022.113811).
- [26] M. A. Tran, T. Komljenovic, J. C. Hulme, M. L. Davenport, and J. E. Bowers, "A robust method for characterization of optical waveguides and couplers," *IEEE Photon. Technol. Lett.*, vol. 28, no. 14, pp. 1517–1520, Jul. 2016, doi: [10.1109/LPT.2016.2556713](https://doi.org/10.1109/LPT.2016.2556713).